Biosensors and Bioelectronics 142 (2019) 111554

Contents lists available at ScienceDirect

Biosensors and Bioelectronics

journal homepage: www.elsevier.com/locate/bios

Competitive electrochemical immunosensor for maduramicin detection by multiple signal amplification strategy *via* hemin@Fe-MIL-88NH$_2$/AuPt

Mei Hu[a,b], Yao Wang[c], Jifei Yang[b], Yaning Sun[b], Guangxu Xing[b], Ruiguang Deng[b], Xiaofei Hu[b,**], Gaiping Zhang[a,b,d,*]

[a] School of Food Science and Technology, Jiangnan University, Wuxi, Jiangsu, 214122, China
[b] Key Laboratory for Animal Immunology of the Ministry of Agriculture, Henan Academy of Agricultural Science, Zhengzhou, 450002, China
[c] College of Food and Bioengineering, Henan University of Science and Technology, Luoyang, 471023, China
[d] Henan Agricultural University, Zhengzhou, 450002, China

ARTICLE INFO

Keywords:
Maduramicin
Metal-organic frameworks
Hemin
Horseradish peroxidase
Hydrogen peroxide
Electrochemical immunosensor

ABSTRACT

Maduramicin (MD) is a type of monoglycoside polyether ionophore antibiotic that can effectively treat coccidiosis and facilitate animal growth. However, its extensive and excessive use brings potential risk to human health. Herein, an electrochemical immunosensor based on indirect competitive format was fabricated for analysis of MD residue in eggs by a multiple signal amplification system. Initially, Au nanoparticles were deposited onto glassy carbon electrode surface to load the coating antigen MD-BSA and to improve conductivity. Then the signal amplification platform was constructed by encapsulating hemin into Fe-MIL-88 NH_2 metal-organic frameworks (hemin@MOFs), and then the obtained composites were decorated with AuPt nanoparticles. The synthesized hemin@MOFs/AuPt was not only used as a signal amplification mediator, but also utilized as a carrier for immobilization of horseradish peroxidase-conjugated affinipure goat anti-mouse antibody (Ab_2-HRP) and horseradish peroxidase (HRP). The constructed hemin@MOFs/AuPt-Ab_2-HRP bioconjugates could effectively amplify the current signal since hemin@MOFs, AuPt and HRP all exhibited high catalytic activity towards the hydrogen peroxide. Moreover, the established immunosensor showed high sensitivity and stability during the detection procedure. With the synergistic catalytic effect of hemin@MOFs, AuPt and HRP, a wide detection range of 0.1–50 ng mL^{-1} and a low detection limit of 0.045 ng mL^{-1} were achieved (S/N = 3), respectively. Ultimately, the developed method displayed excellent performance in practical applications, providing a promising probability to detect other veterinary drug residues to guarantee food safety.

1. Introduction

Maduramicin (MD), a monoglycoside polyether ionophore antibiotic, was isolated from the fermentation product of *Actinomadura yumaensis* (Liu et al., 1983). Due to its board anticoccidial activity and low antibiotic resistance, MD has been widely used to treat coccidiosis in poultry. Since MD can enhance the feed conversion ratio, it has also been extensively used as a feed additive in ruminants (Elwinger et al., 1998). However, its abuse may take potential risk of coronary artery dilatation for human (Huyghebaert et al., 2011). In order to prevent human illness from exposure to MD residues, maximum residue limits (MRLs) have been set in many countries. For example, the MRLs for MD in chicken tissues are typically set as 240–720 μg kg^{-1} in China based on *The Ministry of Agriculture published Announcement 235, China*. In the European Union, MD is forbidden in broiler chickens and turkeys, 12 μg kg^{-1} in eggs and 2 μg kg^{-1} in other animal-derived products. Therefore, in order to guarantee food safety, some desirable detection methods are needed to be designed for monitoring MD residues in animal-derived foods.

Over the past few decades, many well-established analytical methods have been exploited for MD detection. The main detection methods are based on chromatographic analysis which include high-performance liquid chromatography (HPLC) and liquid chromatography-electrospray ionization tandem mass spectrometry (LC-MS/MS) (Barreto et al., 2017; Ha et al., 2016). These approaches are extensively used in the precise chemical analyses for many analytes due to their high accuracy and sensitivity. However, their limitations such as time-consuming, expensive and complex operation are not suitable for on-

* Corresponding author. School of Food Science and Technology, Jiangnan University, Wuxi, Jiangsu, 214122, China.
** Corresponding author.
E-mail addresses: huxf1972@126.com (X. Hu), zhanggaip@126.com (G. Zhang).

https://doi.org/10.1016/j.bios.2019.111554
Received 12 June 2019; Received in revised form 23 July 2019; Accepted 29 July 2019
Available online 31 July 2019

site measurement of MD residues. Enzyme-linked immunosorbent assay (ELISA) is another common analytical method which is applicable in a large number of samples (Guo et al., 2017; Song et al., 2018). Although the ELISA method is widely used and achieves acceptable accurate analytic results, its limited sensitivity impedes its further practical application in some extent. Thus, cost-effective, high-efficiency methods for sensitive detection of MD still remains an urgent need.

Among various analytical methods, the electrochemical immunosensor is considered to be a powerful tool and has attracted growing attention currently (Duran et al., 2019; Trindade et al., 2019), due to its fast response, high sensitivity, simple operation, low cost and high specific recognition ability. To meet the demands of practical use, some nanomaterials which include carbon nanoparticles (Asadian et al., 2019), Au nanoparticles (Liu et al., 2019), MoS_2 nanostructures (Sinha et al., 2018), trimetallic hybrids (Fan et al., 2019) and metal-organic frameworks (MOFs) (Kempahanumakkagari et al., 2018) are devoted to constructing the sensing interface to improve the sensitivity.

Hemin is protoporphyrin IX with a similar peroxidase-like activity as peroxidase enzyme. It is the active center of heme-proteins which include cytochromes, peroxidase, myoglobin and hemoglobin. It has attracted great attention due to its catalyst towards a variety of reduction reactions for H_2O_2, O_2, sulfides and so on (Yang et al., 2017; Ye et al., 2016) through the reversible transformation of Fe(II)/Fe(III) (Genfa and Dasgupta, 1992; Guo et al., 2011). However, its catalytic property is always affected by the oxidative self-degradation in neutral and alkaline aqueous solution (Bruice, 1991). To overcome this shortcoming, hemin often requires its immobilization on high surface area materials to retain the catalytic activity and stability. Many materials have been used as solid supports, including, but not limited to, quantum dots (Freeman et al., 2011), graphene (Zhang et al., 2018), G-quadruplex wrapped glucose oxidase nanocomposites (Li et al., 2015), MoS_2–Au-PEI layered nanocomposites (Yang et al., 2017), and recently MOFs (Cui et al., 2018; Kempahanumakkagari et al., 2018; Li et al., 2018a).

MOFs are a broad class of crystalline porous materials with favorable properties of high surface area, tunable pore size and excellent flexibility (Furukawa et al., 2013), receiving tremendous attention in many fields such as fuel or gas storage and separation (Li et al., 2018), biomedicine (Giménez-Marqués et al., 2016), catalysis (Lee et al., 2009), optoelectronics and sensing (Kreno et al., 2012; Lustig et al., 2017). Recently, many studies have been reported using MOFs as sensitive layer for construction of electrochemical biosensor (Gu et al., 2019; Wang et al., 2019; Zhou et al., 2019). Since their well-ordered porosity structures are available to offer unsaturated coordination bonds and catalytic active sites, MOFs with biomimetic properties are also expected to be appropriate candidates for potential bio-applications (Gkaniatsou et al., 2018). Recently, MOFs with peroxidase catalytic activity have emerged as new versatile biomaterials with similar properties as enzymes (Cui et al., 2018; Kempahanumakkagari et al., 2018; Nath et al., 2016).

Among these applications, a porous MOFs with uniform octahedral shape, Fe-MIL-88NH_2, has attracted increasing attention due to its unique intrinsic peroxidase-like activity (Liu et al., 2013). Especially, the combination of hemin and Fe-MIL-88NH_2 MOFs has become more available in the biological assay because of its higher catalytic efficiency and better biocompatibility and stability in aqueous medium compared with each individual component. While, the low conductivity of MOFs has limited its usage in the field of electrochemical immunosensor, thus it always requires the incorporation of nanomaterials with outstanding electron transfer ability for new or enhanced properties, particularly in conductivity and catalysis (Li et al., 2018b). For instance, gold nanoparticles (AuNPs) and platinum nanoparticles (PtNPs) were reported to be a subset of noble metals with excellent electrical conductivity as well as effective mimicking peroxidase property (He et al., 2013; Zhu et al., 2014; Chen et al., 2018; Xu and Zhang, 2014). Thus, multifunctional hemin@Fe-MIL-88NH_2/metal-based bioconjugates have been performed as signal amplification bioprobes, as evidenced by Au/hemin@MOFs-TBA II–GOD (Xie et al., 2015), Au/hemin@MOFs-DNAzyme (Shao et al., 2018) and hemin-MOFs/PtNPs-SP-BSA (Chen et al., 2017).

In this case, an indirect competitive format electrochemical immunosensor based on AuNPs as GCE modifier and hemin@MOFs/AuPt composites as signal amplification platform was designed and regarded as a high sensitivity and portability device for the detection of MD in real samples. Herein, the multifunctional MOFs-based composites were synthesized by encapsulating hemin into the Fe-MIL-88NH_2 MOFs and then further decorated with AuPt nanoparticles. Next, the obtained hemin@MOFs/AuPt composites were used as carriers of horseradish peroxidase-conjugated affinipure goat anti-mouse antibody (Ab_2-HRP) for the reduction of hydrogen peroxide (H_2O_2) to enhance the sensitivity of the biosensor by the multiple signal amplification performance of hemin@MOFs, AuPt and HRP. Meanwhile, for further improving the catalytic activity and eliminating the nonspecific adsorption, the obtained hemin@MOFs/AuPt-Ab_2-HRP was blocked with HRP instead of traditional bovine serum albumin (BSA). To the best of our knowledge, hemin@Fe-MIL-88NH_2/AuPt-Ab_2-HRP/HRP as bioprobes for fabricating indirect competitive format biosensor was not reported before. In this competitive system, AuNPs were used for immobilizing the coating antigen MD-BSA, then target MD and analyte were competitively bound to the mouse anti-MD monoclonal antibody (Ab_1), finally the bioprobes with high specificity and superior affinity were captured by Ab_1 for signal amplification to detect MD residue. This new biosensor system is anticipated to be a potential tool for trace level analysis of small molecules.

2. Experimental section

The “Reagents and materials” and “Apparatus” are described in Supplementary material.

2.1. Synthesis of Fe-MIL-88NH_2 and hemin@Fe-MIL-88NH_2 (hemin@MOFs)

Fe-MIL-88NH_2 were synthesized by a facile one-step method according to the protocol reported in the literature with some modifications (Liu et al., 2013). Briefly, 0.126 g (0.692 mM) of 2-aminoterephalic acid (NH_2-BDC) and 0.187 g (0.692 mM) of $FeCl_3{\cdot}6H_2O$ were dispersed in 15 mL of N, N-dimethylformamide (DMF), and then 3.45 mM of acetic acid was added into the mixture solution. After stirring for 15 min, the homogeneous mixture was transferred into a 50-mL Teflon-lined stainless-steel autoclave. The sealed autoclave was placed into an air oven and then heated to 120 °C and kept at this temperature for 4 h. After cooling to ambient temperature, the obtained Fe-MIL-88NH_2 MOFs were collected by centrifugation at 10000 rpm for 10 min. To remove the excess reactant, the sediment was washed with DMF and ethanol for three times, respectively. Afterwards, the resultant MOFs were dried in a vacuum oven for overnight at 40 °C. Similarly, the synthesized procedure of hemin@Fe-MIL-88NH_2 MOFs (hemin@MOFs) was the same as above, except that 0.187 g (0.692 mM) of $FeCl_3{\cdot}6H_2O$ was replaced by 0.094 g (0.346 mM) $FeCl_3{\cdot}6H_2O$ and 0.226 g (0.346 mM) hemin according to the literature (Xie et al., 2015).

2.2. Synthesis of hemin@MOFs/AuPt, hemin@MOFs/Au, hemin@MOFs/Pt and MOFs/AuPt

$NaBH_4$ reduction method was used to synthesize hemin@MOFs/AuPt, hemin@MOFs/Au and hemin@MOFs/Pt composites. Typically, 2 mg of hemin@MOFs was dispersed into 1 mL of absolute ethanol and sonicated for 30 min to form a well-dispersed solution. Then 0.5 mL of $HAuCl_4$ ethanol solution (1%, w/v) and 0.5 mL of H_2PtCl_6 ethanol solution (1%, w/v) were consecutively added into the above solution, and sonicated for 20 min. Subsequently, 2 mL of $NaBH_4$ ethanol solution

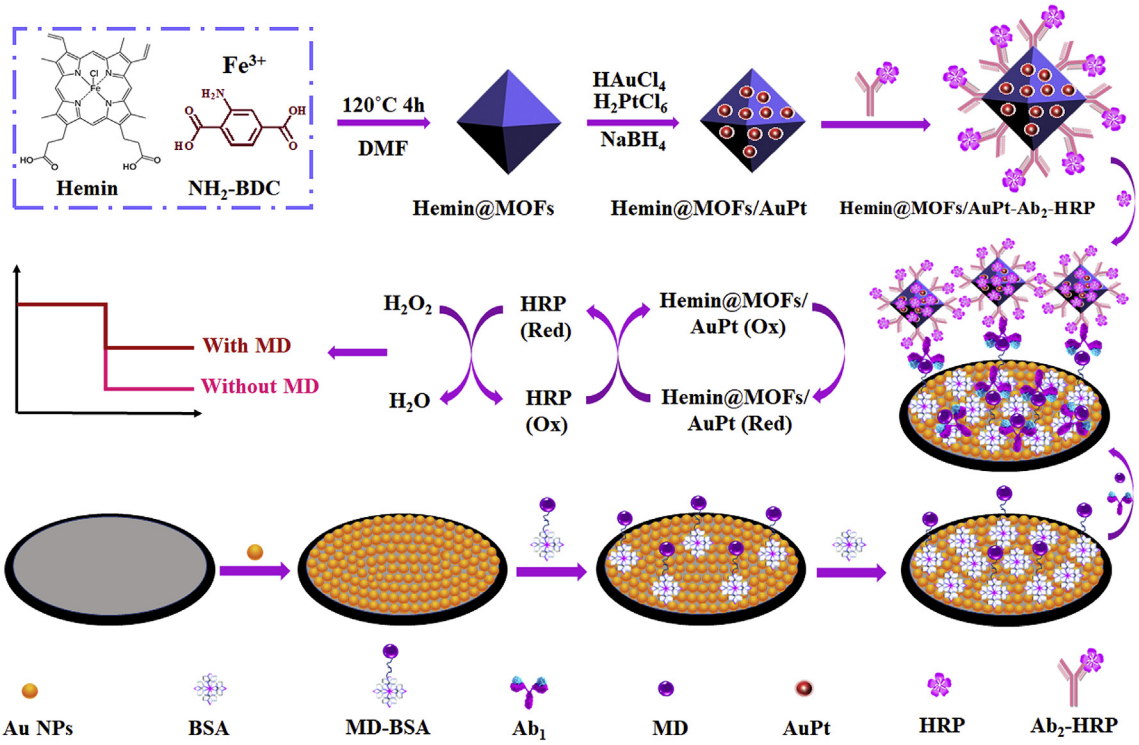

Scheme 1. The preparation of hemin@MOFs/AuPt-Ab2-HRP/HRP bioprobes, the schematic illustration of the proposed competitive electrochemical immunosensor for maduramicin detection and its signal amplification strategy.

(0.6 mM) was added dropwise to the above mixture in an ice-bath. After ultrasonic treatment for 30 min, the mixture was centrifugated at 8000 rpm for 10 min and washed with ultrapure water in successive washing and centrifugation cycles for three times to obtain hemin@MOFs/AuPt composites. Prior to use, the obtained composites were resuspended in 1 mL of phosphate buffer solution (PBS, pH 7.4). The procedure for the synthesis of hemin@MOFs/Au was similar as above, except for that 0.5 mL of H_2PtCl_6 ethanol solution was used instead of 0.5 mL of $HAuCl_4$ ethanol solution, and the same method was applied to the synthesis of hemin@MOFs/Pt by replacing $HAuCl_4$ with H_2PtCl_6. As for MOFs/AuPt, the preparation process was the same as hemin@MOFs/AuPt by replacing the hemin@MOFs with MOFs.

2.3. Preparation of the signal bioprobes–hemin@MOFs/AuPt-Ab_2-HRP/HRP

The preparation process of the hemin@MOFs/AuPt-Ab_2-HRP/HRP signal bioprobes is illustrated in Scheme 1. Briefly, 50 μL of Ab_2-HRP (1:5000 dilution in PBS, pH 7.4) was added dropwise into 1 mL of hemin@MOFs/AuPt composites (2 mg mL^{-1}) by gently stirring at 37 °C for 4 h to obtain the hemin@MOFs/AuPt-Ab_2-HRP bioconjugates. Then the solution was centrifugated to remove the unbound Ab_2-HRP. Afterwards, the obtained bioconjugates were resuspended into 1 mL of HRP solution (1 mg mL^{-1} in PBS, 0.1 M, pH 7.4) and shook for 2 h at 37 °C to block the unreacted active site on the surface of hemin@MOFs/AuPt composites. For comparison, the hemin@MOFs/AuPt-Ab_2-HRP/BSA was also prepared by using 1 mL of BSA solution (1 mg mL^{-1} in PBS) as block agent. Finally, after centrifugation, the achieved signal bioprobes were respectively dispersed into 1 mL of PBS and stored at 4 °C.

2.4. Construction of the competitive electrochemical immunosensor

Scheme 1 demonstrates the construction procedure of the indirect competitive electrochemical immunosensor. Prior to the fabrication of the biosensor, the GCE was polished with 1.0, 0.3 and 0.05 μm alumina powders. After successive washing by sonification in nitric acid/ultrapure water (v/v, 1:1), ethanol and ultrapure water for 2 min respectively, the electrode was dried at room temperature. Then, the AuNPs were electrochemically deposited on the pretreated GCE surface by immersing the electrode into 5 mL of 1.0% $HAuCl_4$ solution at the potential of −0.2 V for 40 s. After rinsing with ultrapure water, 10 μL of MD-BSA (2 μg mL^{-1}) was dropped onto the AuNPs/GCE surface and incubated at 37 °C for 30 min. Thereafter, the AuNPs/GCE was incubated with 50 μL of BSA solution (1 mg mL^{-1} in PBS) at 37 °C for another 30 min to block the nonspecific binding sites. Subsequently, 5 μL of MD solution with a series of concentrations which mixed with 5 μL of Ab_1 (1:10000 dilution in PBS) was added onto the BSA/MD-BSA/AuNPs/GCE at 37 °C for 1 h. Finally, 10 μL of hemin@MOFs/AuPt-Ab_2-HRP/HRP signal bioprobes were cast onto the modified electrode surface for another 1 h at 37 °C to form an immunocomplex biosensing interface. After each step, the modified electrode was washed thoroughly with PBST to remove the unbound attachments. Then the constructed electrochemical immunosensor was stored at 4 °C for future use.

2.5. Electrochemical measurement of MD

The electrochemical characteristics of the modified electrode were tested by cyclic voltammetry (CV) and electrochemical impedance spectroscopy (EIS), each test was conducted in 5.0 mM $[Fe(CN_6)]^{3-/4-}$ solution containing 0.1 M KCl. CV was carried out from −0.2 V to 0.6 V with scan rate at 50 mV s^{-1}, and EIS was analyzed within a frequency range from 0.01 Hz to 100 kHz with amplitude at 5 mV. In order to reduce the background current (Xu et al., 2018), the electrochemical signal was recorded by i-t measurement during the test process with potential at −0.4 V as the starting voltage. After the background current was stable, 4 mM of H_2O_2 was injected into 5 mL of PBS solution (pH 6.0) with constant gentle stirring at room temperature. Egg samples were used to validate the applicability of the prepared electrochemical

immunosensor.

3. Results and discussion

3.1. Sensing mechanism of the fabricated electrochemical immunosensor

The sensing mechanism of the fabricated competitive electrochemical immunosensor was demonstrated in Scheme 1. AuNPs were electrochemically deposited onto the GCE surface as the platform to enhance the conductivity and biocompatibility of the sensing interface. The conductivity of AuNPs could accelerate the electron transfer, thus to improve the sensitivity of the biosensor. Meanwhile, the AuNPs created a larger surface area to offer more active sites for the immobilization of MD-BSA coating antigen *via* Au–NH_2 bond to form a capture layer. Furthermore, due to the high catalytic activity, good chemical stability and large surface area, the as-synthesized hemin@MOFs composites could be employed as a loading platform for anchoring the AuPt nanoparticles and biomolecules, finally used as signal bioprobe. Among them, AuPt was considered as a desirable nanoparticle not only with good biocompatibility and excellent conductivity but also with an excellent catalytic activity than each individual pure PtNPs and pure AuNPs (Manivannan et al., 2017; Xu et al., 2018). Thereafter, Ab_2-HRP and HRP were efficiently immobilized onto the sensing interface of the hemin@MOFs/AuPt composites through the robust Pt–N and/or Au–N bond. Herein, the enzyme-based hemin@MOFs/AuPt-Ab_2-HRP bioconjugates were combined support materials and catalysts within a single composite. In the competitive stage, the immobilized MD and the target MD were competed against each other to acquire Ab_1 *via* antigen-antibody immunoreaction. Subsequently, the hemin@MOFs/AuPt-Ab_2-HRP/HRP signal probes were captured by the immobilized Ab_1. With the presence of H_2O_2, a dramatically amplified electrochemical signal was produced by the reduction reaction due to the synergic catalytic of hemin@MOFs, AuPt and HRP. Thus, the enzyme-assisted multiple signal amplification strategies have improved the sensitivity of the competitive electrochemical immunosensor for the detection of MD in real samples.

3.2. Characterization of the chemical structures and morphologies

To better understand the properties of the synthesized materials, it is necessary to characterize their chemical structures and morphologies. The morphologies of the Fe-MIL-88NH_2 (denoted as MOFs), hemin@Fe-MIL-88NH_2 (denoted as hemin@MOFs) and hemin@Fe-MIL-88NH_2/AuPt (denoted as hemin@MOFs/AuPt) composites were all characterized by using a scanning electron microscope (SEM). As shown in Fig. 1A, the Fe-MIL-88NH_2 MOFs presented a typical crystal morphology of regular octahedron structure, which was approximately consisted with the previous report (Li et al., 2018b). When hemin was introduced, the morphology was slightly changed (Fig. 1B), implying that the encapsulation of hemin into MOFs had impacted the morphology (Shao et al., 2018). As shown in Fig. 1C, a large amount of AuPt nanoparticles were anchored onto the surface of hemin@MOFs, demonstrating that the functionalized hemin@MOFs/AuPt composites were synthesized successfully (Chen et al., 2017).

The transmission electron microscope (TEM) images were investigated by a HT-7700 microscope with an acceleration voltage at 80 kV (Hitachi, Japan). Although SEM observation is helpful to understand the morphology of hemin@MOFs/AuPt composites, it provided very limited information on the small AuPt nanoparticles. In order to learn the detail information, TEM was used to observe the size, distribution and dispersion of the AuPt nanoparticles. From Fig. 1D–F, it can be clearly observed that a large amount of AuPt nanoparticles on diameter at 5–15 nm were anchored onto the surface of the hemin@MOFs. The results were further suggested that the successfully synthesized of the hemin@MOFs/AuPt composites.

As one of the most important characterization techniques, X-ray diffraction (XRD) was adopted to explore the crystalline structure and phase purity of the synthesized MOFs and hemin@MOFs composites. As shown in Fig. 1G, the XRD patterns exhibited diffraction peaks for (002), (101), (103), (200) and (201) planes at 9.03°, 10.4°, 16.4°, 17.8° and 18.6°, respectively, which were in accordance with the typical XRD patterns of Fe-MIL-88NH_2 MOFs reported in literature (Xie et al., 2015). As for hemin@MOFs composites, the XRD patterns showed similar diffractions with Fe-MIL-88NH_2, revealing that the encapsulation of hemin did not affect its crystalline integrity.

To further confirm the successful synthesis of hemin@MOFs/AuPt composites, X-ray photoelectron spectroscopy (XPS) was applied for elemental analysis. As shown in Fig. 1H, the characteristic peaks of Pt4f, Au4f, C1s, N1s, O1s and Fe2p core level regions were obviously discovered. Among them, the peaks of C1s, N1s, O1s and Fe2p indicated the successful synthesis of hemin@Fe-MIL-88NH_2 composites (Xie et al., 2015). For the Au4f spectrum in Fig. 1I, the metallic Au^0 state was proved by the strong energy spectrum peaks of $Au4f_{7/2}$ and $Au4f_{5/2}$ at 83.65 eV and 87.3 eV, respectively. In addition, two pairs of peaks were seen in the Pt4f spectrum from Fig. 1J, here, the peaks at 71.1 eV ($Pt4f_{7/2}$) and 74.35 eV ($Pt4f_{5/2}$) were corresponded to the Pt^0 state, indicating the successful reduction of Pt (IV); and another pair of peaks at 72.65 eV and 75.85 eV were ascribed to the presence of Pt^{2+} species. Notably, the peak intensity of Pt^0 state was dramatically higher than that of Pt^{2+}, implying Pt^0 was predominant. The XPS results revealed that both Au and Pt were in reduced states and anchored onto the hemin@MOFs/AuPt composites.

3.3. Electrochemical performance of the step-wise modified electrode

In order to verify the stepwise modification of the electrochemical immunosensor, electrochemical cyclic voltammetry (CV) and electrochemical impedance spectroscopy (EIS) measurements were all conducted in 5 mM $K_3[Fe(CN)_6]/K_4[Fe(CN)_6]$ solution containing 0.1 M KCl.

The CV was confirmed as an effective approach for observing the redox peak current change of the step-wise modified electrode. In this study, the CV measurements were proceeded with a voltage range from −0.2 V to 0.6 V at a scan rate of 50 mV s^{-1}. As shown in Fig. 2A, bare GCE presented a pair of well-defined reversible redox peaks due to the reversible redox reaction of Fe(II)/Fe(III) (curve a). When the electrode was modified with AuNPs through electrochemical deposition, the redox peak currents obviously increased because of the superior electrical conductivity of AuNPs (curve b). However, the measured peak currents were declined orderly after MD-BSA (curve c), BSA (curve d) and Ab_1 (curve e) were incubated onto the modified electrode. This was ascribed to the electron hinderance properties of the bioactive substances, suggesting that the non-conductive MD-BSA, BSA and Ab_1 were all immobilized on the AuNPs/GCE surface. Finally, when the hemin@MOFs/AuPt-Ab_2-HRP/HRP bioprobes were attached on the modified electrode, the peak currents were increased (curve f) due to the excellent conductivity of the AuPt nanoparticles anchored onto the hemin@MOFs surface. These results approved that the MD electrochemical immunosensor was successfully constructed.

EIS was further used to validate the modification processes and sensing interface properties of the proposed biosensor. It was inferred by the impedance change in the Nyquist plot, which included a semicircle portion at higher frequency corresponded to the electron transfer resistance process (R*et*) and a linear portion at lower frequency subjected to the diffusion process (Li et al., 2018b). As shown in Fig. 2B, it was observed that the electron transfer resistance displayed a small semicircle with bare GCE (curve a), which exhibited a R_{et} value at 341.5 Ω, indicating its good conductivity. When AuNPs with remarkable electrical transport property were electrodeposited onto the electrode, the resistance was declined to almost a straight line (curve b), the R_{et} value was decreased dramatically to 48.47 Ω. After MD-BAS (curve c), BSA (curve d) and Ab_1 (curve e) were sequentially incubated onto

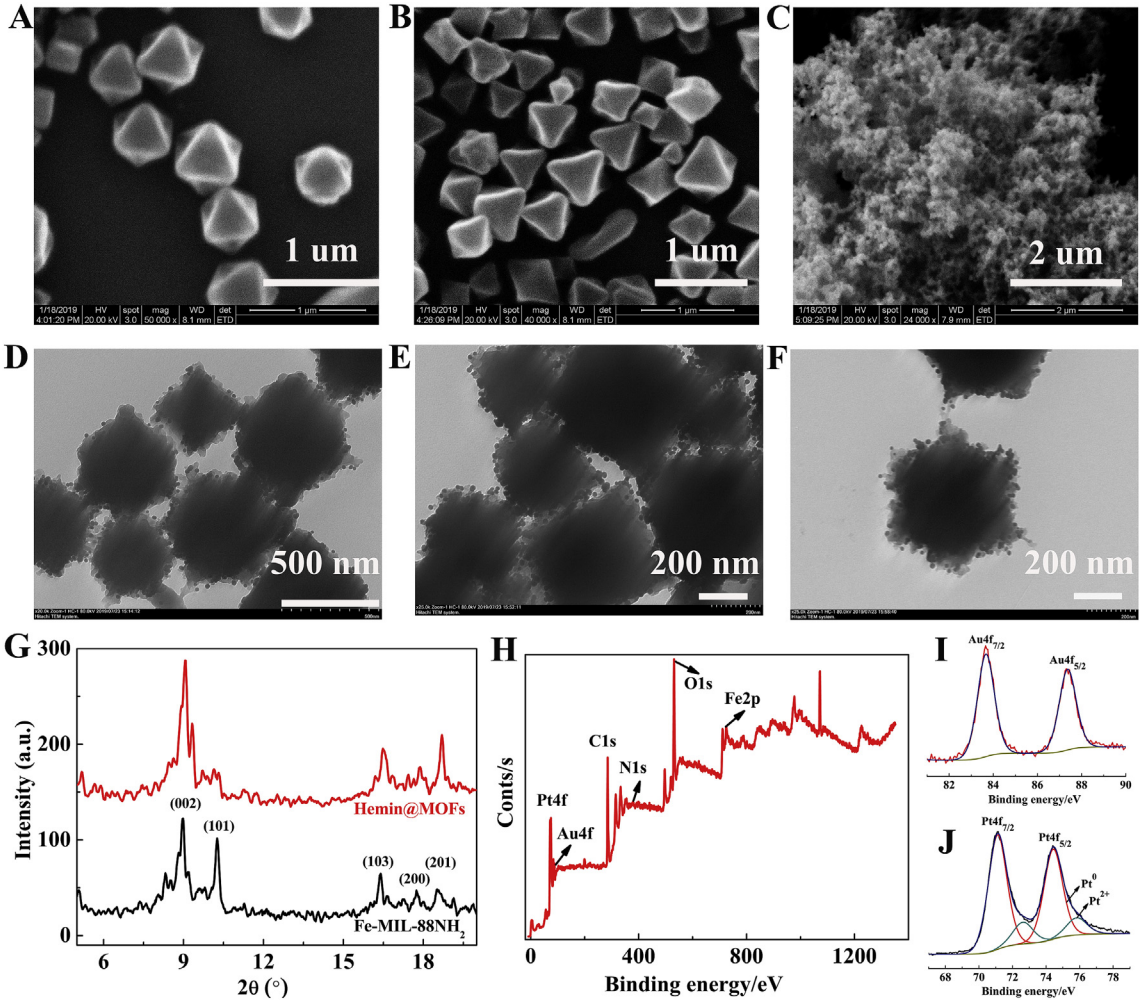

Fig. 1. Scanning electron microscope images of Fe-MIL-88NH_2 (A), hemin@Fe-MIL-88NH_2 (B) and hemin@Fe-MIL-88NH_2/AuPt (C). Transmission electron microscope images of hemin@Fe-MIL-88NH_2/AuPt (D–F). (G) X-ray diffraction patterns of Fe-MIL-88NH_2 MOFs and hemin@MOFs. (H) The X-ray photoelectron spectroscopy of hemin@MOF/AuPt composites. (I) The spectrum of Au4f in hemin@MOF/AuPt composites. (J) The spectrum of Pt4f, Pt^0 and Pt^{2+} in hemin@MOF/AuPt composites.

the modified electrode, the *Ret* were successively increased to 102 Ω, 501 Ω and 663 Ω because of the blocking effect of the bioactive substances, denoting that the formed immunocomplex obstructed the electron transfer ability. Subsequently, with the capturing of the hemin@MOFs/AuPt-Ab_2-HRP/HRP signal bioprobes by Ab_1 (curve f), R*et* was decreased to 596 Ω because the conductivity of AuPt on the hemin@MOFs composites had enhanced the electron transfer efficiency between the electrode interface and redox probe solution. The obtained EIS results in accordance with the CV results further proved the successful construction of the electrochemical immunosensor.

3.4. Amplification strategies of different signal bioprobes

To confirm the signal amplification strategies of the competitive electrochemical immunosensor, different signal bioprobes were used as control groups for the reduction of H_2O_2 at −0.4 V in PBS (pH 6.0). The signal probes were comprised of hemin@MOFs/AuPt-Ab_2-HRP/HRP, MOFs/AuPt-Ab_2-HRP/HRP, hemin@MOFs/Au-Ab_2-HRP/HRP, hemin@MOFs/Pt-Ab_2-HRP/HRP and hemin@MOFs/AuPt-Ab_2-HRP/BSA.

As shown in Fig. 3A, compared to the immunosensor incubated with MOFs/AuPt-Ab_2-HRP/HRP (b), the signal bioprobes of hemin@MOFs/

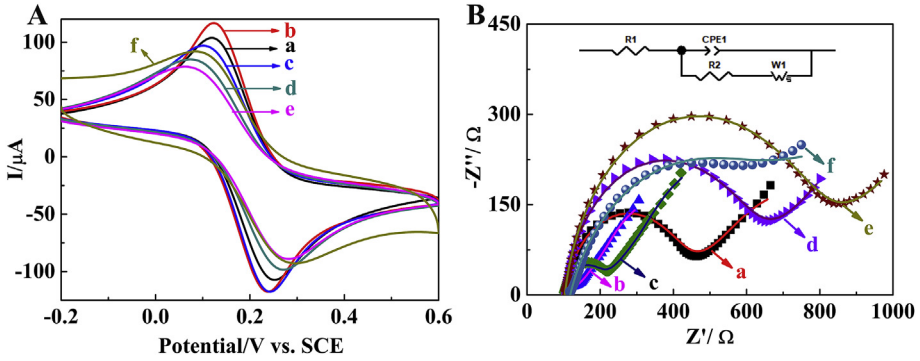

Fig. 2. Electrochemical cyclic voltammetry (A) and electrochemical impedance spectroscopy (B) characterization of the stepwise modified electrode in 5 mM $[Fe(CN)_6]^{3-/4-}$ solution containing 0.1 M KCl: (a) Bare GCE, (b) AuNPs/GCE, (c) MD-BSA/AuNPs/GCE, (d) BSA/MD-BSA/AuNPs/GCE, (e) Ab_1/BSA/MD-BSA/AuNPs/GCE, (f) Hemin@MOs/AuPt-Ab_2-HRP/HRP/Ab_1/BSA/MD-BSA/AuNPs/GCE.

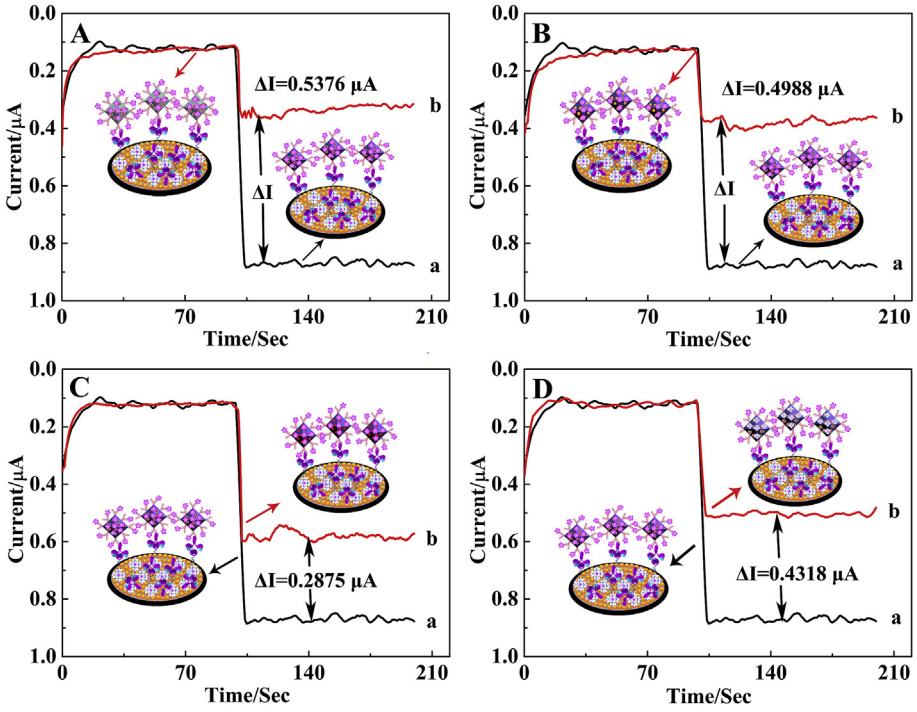

Fig. 3. The i-t curves of the as-prepared competitive electrochemical immunosensor incubated with different signal bioprobes: (A) Hemin@MOFs/AuPt-Ab_2-HRP/HRP (a) and MOFs/AuPt-Ab_2-HRP/HRP (b); (B) Hemin@MOFs/AuPt-Ab_2-HRP/HRP (a) and hemin@MOFs/Au-Ab_2-HRP/HRP (b); (C) Hemin@MOFs/AuPt-Ab_2-HRP/HRP (a) and hemin@MOFs/Pt-Ab_2-HRP/HRP (b); (D) Hemin@MOFs/AuPt-Ab_2-HRP/HRP (a) and hemin@MOFs/AuPt-Ab_2-HRP/BSA (b).

AuPt-Ab_2-HRP/HRP (a) displayed a higher current enhancement owing to the synergistic catalysis effect of hemin@MOFs, AuPt and HRP towards H_2O_2. In Fig. 3B, the hemin@MOFs/Au-Ab_2-HRP/HRP (a) showed a lower current than that of hemin@MOFs/AuPt-Ab_2-HRP/HRP (b) as well as hemin@MOFs/Pt-Ab_2-HRP/HRP (b) (Fig. 3C). This was attributed to the superior electrocatalytic performance of AuPt, which could vigorously catalyze the reduction of H_2O_2 and enhance the current response of electrochemical signal, undoubtedly, greater than each individual AuNPs and PtNPs. As previously mentioned, to eliminate the possible remaining active sites, BSA was generally used as blocking agent. However, the signal bioprobes modified by BSA reduced the sensitivity of the biosensors as BSA possessed non-catalytic activity towards H_2O_2 decreasing the i-t current signal. In contrast, HRP could trigger the bioelectrocatalytic reduction of H_2O_2 when used as the blocking agent. Therefore, the current response of hemin@MOFs/AuPt-Ab_2-HRP/HRP (a) was much higher than that of hemin@MOFs/AuPt-Ab_2-HRP/BSA (b) as shown in Fig. 3D. These results manifested that the current signal amplification was ascribed to the synergistic effect of the enzyme and the synthesized composites. The multiple signal amplify strategy was successfully implemented, which significantly enhanced the sensitivity of the proposed electrochemical immunosensor.

3.5. Optimization of experimental conditions

To obtain a superior analytical performance with high sensitivity and selectivity of the proposed competitive-type immunosensor for MD detection, some certain crucial experimental parameters were optimized under the same conditions, including the electrodeposition time of AuNPs, the concentration of coating antigen MD-BSA, the pH of PBS and the concentration of H_2O_2.

AuNPs electrodeposition time was an important factor for providing a beneficial surface area to immobilize the coating antigen. As shown in Fig. S1A (see the Supplementary material), the current change was increased distinctly with the increase of the deposition time from 10 to 40 s. Then the current was slightly decreased as prolonging the deposition time after 40 s. This was because the excessive amount of AuNPs could hinder the electron transfer, thus decreased the current response, which was consistent with the previous study (Wu et al., 2013). Hence, 40 s was selected as the optimal electrodeposition time for the AuNPs.

Since coating antigen (*i.e.* MD-BSA) was also a considerable parameter affecting the performance of the biosensor, the concentration of MD-BSA was investigated. The much higher amount of MD-BSA could attach a larger number of Ab_1, which then captured more hemin@MOFs/AuPt-Ab_2-HRP/HRP bioprobes to generate a higher i-t current response. While, excess MD-BSA could prevent the electron transfer. Thus, the MD-BSA concentrations ranged from 0.5 μg mL^{-1} to 8 μg mL^{-1} (0.5, 1, 2, 4, 8 μg mL^{-1}) was carefully examined. As shown in Fig. S1B, the current was significantly enhanced with the increasing of MD-BSA concentration and reached maximum value at 2 μg mL^{-1}. Therefore, the suitable MD-BSA concentration at 2 μg mL^{-1} was adopted to construct the immunosensor.

The pH of the PBS solution had a great influence on the biological activity and catalytic ability of the immunosensor since the immobilized proteins and composites were probably influenced by alkaline or acid solutions. Considering the stability and activity of proteins, the impact of pH was investigated within the range of 5.0–9.0 in PBS solution by i-t measurement. As shown in Fig. S1C, the amperometric signal of the immunosensor increased with the pH varying from 4.97 to 5.98, reaching the maximum signal response at pH 5.98 which was approximately approached pH 6.0, and then decreased with further increasing the pH from 5.98 to 8.97. Obviously, the bioactivity of the antigen-antibody attachment was declined under highly acidic or alkaline environments (Chen et al., 2019). Thereby, pH 6.0 was chosen as the optimal condition for the subsequent experiments.

Since H_2O_2 was catalyzed by the synergic effect of hemin@MOFs/AuPt composites and HRP to amplify the amperometric signal, it was necessary to explore its optimum concentration as well. The concentrations of the injected H_2O_2 varied from 1 mM to 5 mM. As shown in Fig. S1D, the signal response increased distinctly with the addition of H_2O_2 in the range of 1 mM–4 mM and then decreased, demonstrating that the best electrocatalysis property was achieved at 4 mM. Thus, 4 mM of H_2O_2 was selected as the optimal concentration throughout the measurement.

3.6. Analytical performance of the immunosensor for MD detection

The as-prepared competitive electrochemical immunosensor was

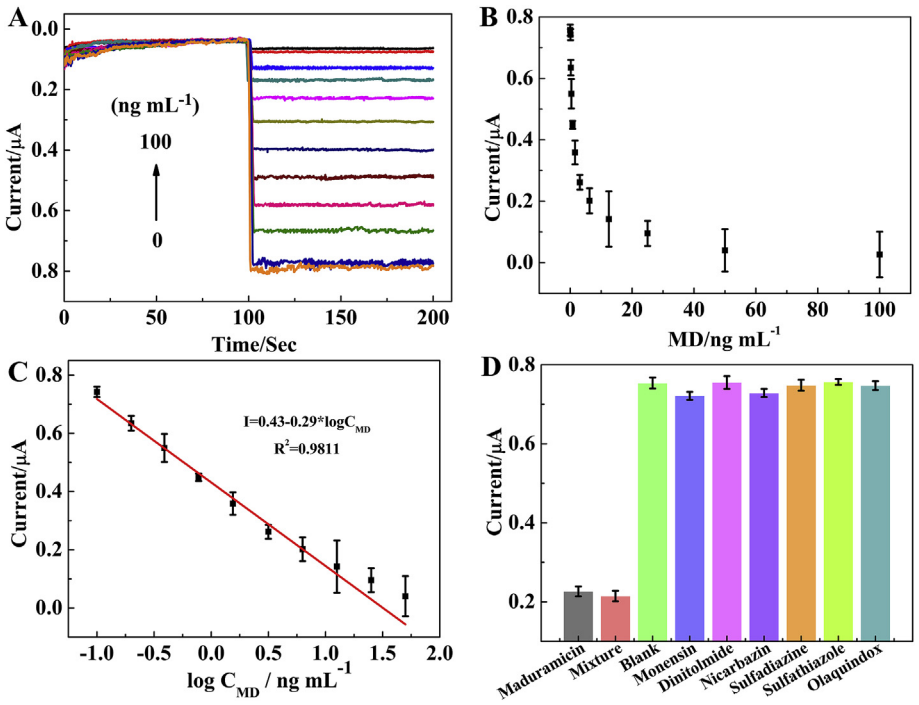

Fig. 4. (A) The i-t curve signals of the fabricated competitive electrochemical immunosensor for the detection of different concentrations of MD from 0–100 ng mL^{-1}. (B) The current values of the proposed immunosensor with different MD concentrations. (C) The calibration plot of the current response *vs.* lgC$_{MD}$ within the linear range from 0.1–50 ng mL^{-1}. (D) Selectivity of the electrochemical immunosensor towards 5 ng mL^{-1} MD, 5 ng mL^{-1} MD + 50 ng mL^{-1} per interfering substance, 0 ng mL^{-1} analyte, 50 ng mL^{-1} monensin, 50 ng mL^{-1} dinitolmide, 50 ng mL^{-1} nicarbazin, 50 ng mL^{-1} sulfathiazole and 50 ng mL^{-1} olaquindox (error bars: SD, n = 3).

conducted to detect different concentrations of MD within the range from 0 ng mL^{-1} to 100 ng mL^{-1} (*i.e.* 0, 0.1, 0.2, 0.39, 0.78, 1.56, 3.125, 6.25, 12.5, 25, 50, 100 ng mL^{-1}) under the optimal conditions. The measurements were conducted in PBS at −0.4 V by i-t curves in Fig. 4A and the current intensities were recorded (Fig. 4B). Notably, the electrochemical signal exhibited a regular change with the variation of MD concentrations. During the indirect competitive immunoassay format, AuNPs/GCE provided the solid support for adsorption of coating antigen MD-BSA, then the modified interface was exposed to a mixed solution with different concentrations of target MD and a certain amount of Ab_1, thereafter the fixed MD and free MD competed for a limited number of antibody binding sites. After the electrode was modified with proteins layer by layer, the i-t current was too tiny to provide an effective approach for the target analyte determination. In order to enhance the sensitivity of the biosensor, the hemin@MOFs/AuPt-Ab_2-HRP/HRP bioprobes were captured by the immobilized Ab_1 to catalyze H_2O_2 to amplify the signal response. Thus, quantitative analysis was performed by determining the current value generated from the synergetic catalytic amplification performance of the bioprobes. With a certain amount of MD-BSA, a lower signal was generated at higher MD concentration. In contrast, larger signal was created at a lower MD concentration. Namely, the current signal produced by the bioprobes was inversely proportional to the target MD concentration. In Fig. 4C, the timing current response values presented a good linear relationship with the logarithm of MD concentrations from 0.1 to 50 ng mL^{-1}. The regression equation of the calibration plot was fitted to be I (μA) = 0.43–0.29*log C$_{MD}$ (ng mL^{-1}) (R^2 = 0.9811) with a detection limit of 0.045 ng mL^{-1} (S/N = 3). The designed biosensor displayed an extremely low detection limit due to high specificity and robust affinity between MD and Ab_1, and the excellent catalytic ability towards H_2O_2 of the bioprobes. The analytical performance indicated the feasibility of the electrochemical immunosensor for quantitative detection of MD.

Compared with previously reported studies for MD detection (Table S1), the proposed competitive electrochemical immunosensor based on the hemin@MOFs/AuPt-Ab_2-HRP/HRP bioprobes exhibited an excellent analytical performance with a superior sensitivity and a low LOD. These predominant sensing properties of the constructed platform is mainly ascribed to the following reasons: (i) the prepared hemin@MOFs hybrids possessed high catalytic ability towards H_2O_2; (ii) the high specific area of the hemin@MOFs hybrids provided a plenty of active sites which could load a large amount of AuPt nanoparticles (AuPtNPs) on the surface; (iii) the loaded AuPt NPs not only enhanced the catalytic performance of the composites, but also provided abundant binding sites for HRP and Ab_2-HRP biomolecules immobilization, thus obtained high sensitive bioprobes; (iv) the co-synergistic catalysis effect of hemin@MOFs, AuPt and HRP triggered a multiple signal amplification system, which greatly increased the sensitivity of the immunosensor. The results were indicated that the developed biosensor displayed better analytical performance.

3.7. Reproducibility, stability and selectivity

To verify the reproducibility of the immunosensor, i-t responses were recorded under the same condition. Each sample was assessed by 5 different immunosensors which were constructed by using the same protocol. The measurements recorded at 5 ng mL^{-1} of MD yielded the relative standard deviation (RSD) value at 2.5% (Fig. S2), confirming the reliability of the reproducibility. Additionally, the storage stability of the biosensor was also evaluated. The immunosensors were prepared in parallel and then stored at 4 °C and tested within 10 days. The highly stable response was observed over these 10-day periods with an RSD of 7.3% (Fig. S3), demonstrating that such storage could meet the demand of stability for MD detection.

Furthermore, the selectivity of the immunosensor was also an essential property for its application. Here, we compared the target MD *vs.* nontarget interfering substances including monensin, dinitolmide, nicarbazin, sulfadiazine, sulfathiazole and olaquindox. The tests were divided into nine groups and each group was repeated for three times in parallel. The first group was MD at 5 ng mL^{-1}, the second group was the mixture of MD at 5 ng mL^{-1} and each interfering substance at 50 ng mL^{-1}, the third group was blank control trial, and the other six groups were interfering substances at 50 ng mL^{-1} respectively. The results were depicted in Fig. 4D. It was definitely observed that there were no significant changes in the signal response between the target MD and the mixture. Meanwhile, even at 10-fold higher concentrations than that of MD, no distinct signal changes of the interfering substances were found compared to the current from the blank group. These results

confirmed that the fabricated immunosensor possessed an excellent selectivity towards MD, based on the specific recognition of antigen and antibody.

3.8. Practical application

Eggs were purchased from the local market and initially prepared by mixing the egg white and yolk with a high-speed blender. Then 2.0 g of homogenized egg sample was extracted with 10 mL ethanol. After centrifugation, the precipitate was extracted for the second time as previous procedure. Then the supernatant was collected together and evaporated to dryness under the nitrogen stream. Next, the residue was dissolved in 10 mL of ethanol/PBS (0.1 M, pH 7.4) (5:95, v/v) and filtrated by a 0.22 μm filtering membrane for the following analysis.

In order to verify the feasibility of the established biosensor in real sample detection, various concentrations of target MD were added into the pretreated egg samples which were confirmed to be negative of MD by HPLC-MS/MS. Then the recovery experiments were applied to detect the egg samples spiked with 0.5 ng mL^{-1}, 5 ng mL^{-1} and 10 ng mL^{-1} of MD, respectively. The recoveries were calculated to be 96.4% ~ 106% and the RSD was 2.9% ~ 3.5%, respectively (Table S2), suggesting that the developed electrochemical immunosensor provided a reliable alternative for the detection of MD in practical applications.

4. Conclusion

In this study, we presented an indirect competitive electrochemical immunosensor to detect MD residue. The enzyme-assistant (*i.e.* HRP) cooperative catalysis signal amplification strategy based on hemin@Fe-MIL-88NH_2/AuPt composites were first successfully designed and exhibited remarkable electrocatalytic activity towards H_2O_2. The Fe-MIL-88NH_2 was served as the carrier platform to encapsulate hemin to enhance its catalysis property and stability, then the prepared hemin@MOFs were further anchored by AuPt nanoparticles, which was used to capture the Ab_2-HRP and HRP to obtain the signal amplification bioprobes. Due to the synergic catalytic effect, the sensing platform offers considerable multiple signal amplification. With these performances, the electrochemical biosensor based on the indirect competitive immunoassay format showed a low detection limit of 0.045 ng mL^{-1}, satisfying the application for ultrasensitive detection of MD. Ultimately, such electrochemical immunosensor opened up new possibilities for the point-of-care screening of various veterinary drugs residual in food samples. Nevertheless, a little high RSD of 7.3% in the period of 10-day revealed that the proposed biosensor may not suitable for a long-term storage though it possessed ultrahigh sensitivity. To solve this problem is still a challenge, requiring an in-depth study in the future work.

Declaration of competing interest

The authors declare that they have no known competing financial interests or personal relationships that could have appeared to influence the work reported in this paper.

CRediT authorship contribution statement

Mei Hu: Conceptualization, Methodology, Software, Investigation, Formal analysis, Writing - original draft, Writing - review & editing. **Yao Wang:** Formal analysis. **Jifei Yang:** Formal analysis. **Yaning Sun:** Funding acquisition. **Guangxu Xing:** Supervision. **Ruiguang Deng:** Supervision. **Xiaofei Hu:** Supervision, Funding acquisition. **Gaiping Zhang:** Conceptualization, Supervision, Project administration, Investigation, Resources.

Acknowledgments

This work was funded by China Postdoctoral Science Foundation Funded Project (2018M632778) and National Science & Technology Pillar Program of "12th Five Year Plan" (2014BAD13B05).

Appendix A. Supplementary data

Supplementary data to this article can be found online at https://doi.org/10.1016/j.bios.2019.111554.

References

Asadian, E., Ghalkhani, M., Shahrokhian, S., 2019. Sens. Actuators B Chem. 293, 183–209.
Barreto, F., Ribeiro, C., Hoff, R.B., Costa, T.D., 2017. Talanta 168, 43–51.
Bruice, T.C., 1991. Accounts Chem. Res. 24 (8), 243–249.
Chen, H., Qiu, Q., Sharif, S., Ying, S., Wang, Y., Ying, Y., 2018. ACS Appl. Mater. Interfaces 10 (28), 24108–24115.
Chen, J., Yu, C., Zhao, Y., Niu, Y., Zhang, L., Yu, Y., Wu, J., He, J., 2017. Biosens. Bioelectron. 91, 892–899.
Chen, Y., Wang, A.-J., Yuan, P.-X., Luo, X., Xue, Y., Feng, J.-J., 2019. Biosens. Bioelectron. 132, 294–301.
Cui, J., Ren, S., Sun, B., Jia, S., 2018. Coord. Chem. Rev. 370, 22–41.
Duran, B.G., Castañeda, E., Armijo, F., 2019. Biosens. Bioelectron. 131, 171–177.
Elwinger, K., Berndtson, E., Engstrom, B., Fossum, O., Waldenstedt, L., 1998. Acta Vet. Scand. 39 (4), 433–441.
Fan, L., Yan, Y., Guo, B., Zhao, M., Li, J., Bian, X., Wu, H., Cheng, W., Ding, S., 2019. Sens. Actuators B Chem. 126697.
Freeman, R., Liu, X., Willner, I., 2011. J. Am. Chem. Soc. 133 (30), 11597–11604.
Furukawa, H., Cordova, K.E., O'Keeffe, M., Yaghi, O.M., 2013. Science 341 (6149), 1230444.
Genfa, Z., Dasgupta, P.K., 1992. Anal. Chem. 64 (5), 517–522.
Giménez-Marqués, M., Hidalgo, T., Serre, C., Horcajada, P., 2016. Coord. Chem. Rev. 307, 342–360.
Gkaniatsou, E., Sicard, C., Ricoux, R., Benahmed, L., Bourdreux, F., Zhang, Q., Serre, C., Mahy, J.P., Steunou, N., 2018. Angew. Chem., Int. Ed. Engl. 130 (49), 16373–16378.
Gu, C., Guo, C., Li, Z., Wang, M., Zhou, N., He, L., Zhang, Z., Du, M., 2019. Biosens. Bioelectron. 134, 8–15.
Guo, L., Xu, L., Song, S., Liu, L., Kuang, H., 2017. Food Agric. Immunol. 29 (1), 458–469.
Guo, Y., Deng, L., Li, J., Guo, S., Wang, E., Dong, S., 2011. ACS Nano 5 (2), 1282–1290.
Ha, J., Song, G., Ai, L.F., Li, J.C., 2016. J. Chromatogr. B 1017–1018, 187–194.
He, W., Zhou, Y.T., Wamer, W.G., Hu, X., Wu, X., Zheng, Z., Boudreau, M.D., Yin, J.J., 2013. Biomaterials 34 (3), 765–773.
Huyghebaert, G., Ducatelle, R., Van Immerseel, F., 2011. Vet. J. 187 (2), 182–188.
Kempahanumakkagari, S., Kumar, V., Samaddar, P., Kumar, P., Ramakrishnappa, T., Kim, K.H., 2018. Biotechnol. Adv. 36 (2), 467–481.
Kreno, L.E., Leong, K., Farha, O.K., Allendorf, M., Van Duyne, R.P., Hupp, J.T., 2012. Chem. Rev. 112 (2), 1105–1125.
Lee, J., Farha, O.K., Roberts, J., Scheidt, K.A., Nguyen, S.T., Hupp, J.T., 2009. Chem. Soc. Rev. 38 (5), 1450–1459.
Li, H., Wang, k., Sun, Y., Lollar, C., Li, J., Zhou, H., 2018. Mater. Today 21 (2), 108–121.
Li, S., Liu, X., Chai, H., Huang, Y., 2018a. Trac. Trends Anal. Chem. 105, 391–403.
Li, Y., Deng, J., Fang, L., Yu, K., Huang, H., Jiang, L., Liang, W., Zheng, J., 2015. Biosens. Bioelectron. 63, 1–6.
Li, Y., Yu, C., Yang, B., Liu, Z., Xia, P., Wang, Q., 2018b. Biosens. Bioelectron. 102, 307–315.
Liu, C., Hermann, T.E., Downey, A., Prosser, B.L.T., Schildknecht, E., Palleroni, N.J., Westley, J.W., Miller, P.A., 1983. J. Antibiot. 36 (4), 343–350.
Liu, Y.L., Zhao, X.J., Yang, X.X., Li, Y.F., 2013. Analyst 138 (16), 4526–4531.
Liu, Q., Yang, T., Ye, Y., Chen, P., Ren, X., Rao, A., Wan, Y., Wang, B., Luo, Z., 2019. J. Mater. Chem. B 7 (9), 1442–1449.
Lustig, W.P., Mukherjee, S., Rudd, N.D., Desai, A.V., Li, J., Ghosh, S.K., 2017. Chem. Soc. Rev. 46 (11), 3242–3285.
Manivannan, S., Kang, I., Seo, Y., Jin, H.E., Lee, S.W., Kim, K., 2017. ACS Appl. Mater. Interfaces 9 (38), 32965–32976.
Nath, I., Chakraborty, J., Verpoort, F., 2016. Chem. Soc. Rev. 45 (15), 4127–4170.
Shao, K., Wang, B., Nie, A., Ye, S., Ma, J., Li, Z., Lv, Z., Han, H., 2018. Biosens. Bioelectron. 118, 160–166.
Sinha, A., Tan, B., Huang, Y., 2018. Trac. Trends Anal. Chem. 102, 75–90.
Song, M., Xiao, Z., Xue, Y., Zhang, X., Ding, S., Li, J., 2018. Food Agric. Immunol. 29 (1), 590–599.
Trindade, E.K.G., Silva, B.V.M., Dutra, R.F., 2019. Biosens. Bioelectron. 138, 111311.
Wang, M., Hu, M., Hu, B., Guo, C., Song, Y., Jia, Q., He, L., Zhang, Z., Fang, S., 2019. Biosens. Bioelectron. 135, 22–29.
Wu, Y., Xu, W., Wang, Y., Yuan, Y., Yuan, R., 2013. Electrochim. Acta 88, 135–140.
Xie, S., Ye, J., Yuan, Y., Chai, Y., Yuan, R., 2015. Nanoscale 7 (43), 18232–18238.
Xu, W., Qin, Z., Hao, Y., He, Q., Chen, S., Zhang, Z., Peng, D., Wen, H., Chen, J., Qiu, J., Li, C., 2018. Biosens. Bioelectron. 113, 148–156.
Xu, Y., Zhang, B., 2014. Chem. Soc. Rev. 43 (8), 2439–2450.
Yang, Y., Zhang, H., Huang, C., Yang, D., Jia, N., 2017. Biosens. Bioelectron. 89, 461–467.
Ye, Y., Gao, J., Zhuang, H., Zheng, H., Sun, H., Ye, Y., Xu, X., Cao, X., 2016. Microchim. Acta 184 (1), 245–252.
Zhang, G., Liu, Z., Fan, L., Guo, Y., 2018. Mikrochim. Acta 185 (3), 159.
Zhu, J., Xu, Z., Lu, B., 2014. Nano Energy 7, 114–123.
Zhou, N., Su, F., Guo, C., He, L., Jia, Z., Wang, M., Jia, Q., Zhang, Z., Lu, S., 2019. Biosens. Bioelectron. 123, 51–58.